Engineering and Technology Journal
Journal homepage: https://etj.uotechnology.edu.iq

Electromagnetic analysis of a surface-mounted permanent magnet motor

TA Ayorinde [a,b,c*], **PF Le Roux** [d], **T Jamiru** [a]

[a] Department of Mechanical and Mechatronics Engineering, Tshwane University of Technology, South Africa.
[b] National Biotechnology Research and Development Agency, Abuja, Nigeria.
[c] Department of Agricultural and Environmental Engineering, Obafemi Awolowo University, Ile-Ife, Nigeria.
[d] Department of Electrical Engineering, Tshwane University of Technology, South Africa.
*Corresponding author Email: ayorindeadedayo@gmail.com

HIGHLIGHTS

- The electromagnetic field of a surface-mounted permanent magnet motor (SMPMM) was modeled using finite element analysis
- Magnetic performance parameters were evaluated under current excitations up to 2 A, and saturation in laminated steel was revealed
- A maximum torque of 1.88 N.m was achieved at an optimal air gap of 0.45 mm
- Core and eddy current losses were computed to quantify high-frequency effects
- Experimental validation with M36, 65C600, EN8, and EN353 confirmed the significance of nonlinear material properties for high-efficiency design

Keywords:
Surface-mounted permanent magnet; Flux linkage; Self-inductance; Mutual inductance.

ABSTRACT

This study investigates the finite element analysis (FEA) of a surface-mounted permanent magnet motor (SMPMM) using QuickField software. The model was developed by solving Maxwell's equations on meshed SMPMM geometries, integrating real B-H curve data for laminated steel stator and rotor materials to accurately represent the nonlinear behaviour of the SMPMM. The simulation was performed to evaluate the magnetic flux distribution, air-gap flux density, torque, and self-and mutual inductance at an operational speed of 3000 rpm, and compares the simulated outputs with existing experimental results. Under current excitation up to 2 A, the simulated air gap density ranged from 0.7 Tesla (T) at minimum rotor-stator coupling to 1.2 T at peak alignment during an electrical cycle. Peak torque reached 1.8823 N.m at a 0.45 mm air gap, decreasing slightly to 1.8572 N.m at 0.75 mm. Self-inductance declined from 0.8 H to 0.5 H, while mutual inductance declined from 0.049 H to 0.03 H, showing the effect of magnetic saturation. Core and eddy current losses increased nonlinearly at higher speeds and flux densities. The validated results highlight the importance of incorporating nonlinear magnetic properties and velocity-dependent losses in SMPMM design accurate prediction of performance under both nominal and extreme conditions, supporting robust, high-efficiency motor development for industrial, automotive, and renewable energy applications.

1. Introduction

Industrialization is on a new pedestal with the advent of Industry 5.0, which is based on human-centered innovation, creativity with efficiency, artificial intelligence, and machine precision in industrial production [1]. Recently, permanent magnet motors have become a crucial technology in the rapidly growing power electronics industry [2], serving as a power drive in various applications, such as industrial automation, agricultural equipment, electric vehicles, robots, renewable energy systems, and high-speed industrial operations [3]. Surface-mounted permanent magnetic motors (SMPMMs) are valued for their compact size, high torque density, and high efficiency [4,5]. However, the nonlinear magnetic characteristics and electromagnetic losses in rapid and dynamic situations have been identified as major determinants of permanent magnet performance [6]. Studies have shown that designs and analyses commonly include magnetic fields under a limited flux density while neglecting speed-dependent dynamic losses [7]. Consequently, these models do not adequately capture core saturation effects or eddy current losses at higher operating speeds [8,9].

Several magnet types, including NdFeB, SmCo, and ferrite, have been studied in the past, each with distinct performance traits [10-12]. High-energy magnets, such as SmCo, offer superior flux density and thermal stability, making them ideal for high-speed and high-temperature applications [13-15]. However, the high procurement costs and limited availability of cobalt for numerous applications have spurred interest in alternatives [16,17]. Strontium ferrite (Sr–ferrite No. 8), while offering lower magnetic performance, provides a cost-effective solution for applications with moderate performance requirements [18]. This trade-off between cost and magnetic capability continues to drive research into optimized motor designs using various permanent-magnet materials.

http://doi.org/10.30684/etj.2025.163298.1992
Received 25 July 2025; Received in revised form 12 August 2025; Accepted 22 August 2025; Available online 30 August 2025
2412-0758/University of Technology-Iraq, Baghdad, Iraq

Research by Slemon [19], also suggests that SMPMM with neodymium-iron-boron (Nd-Fe-B) magnets are capable of high torque performance, making them an ideal alternative for advanced industrial and automotive applications. However, high stator currents render the magnet susceptible to demagnetization, particularly under low-duty-factor conditions when short bursts of high performance are required. In contrast, high-duty factor applications, where long-duration operation is required, require thermal management to maintain the optimal performance of the magnet. Liquid cooling, heat sinks, and forced-air cooling systems are also required to prevent overheating and winding insulation in magnets. Handling the interaction between thermal and electromagnetic limitations is essential because overheating may lead to insulation, impair magnetic flux, and reduce system efficiency [20,21]. Hence, there is a need to simulate models that incorporate realistic nonlinear magnetic properties and account for high-frequency loss mechanisms to ensure reliable and efficient motor operation.

Finite Element Analysis (FEA) offers a robust solution to these challenges by solving Maxwell's equations in complex geometries with realistic material properties using QuickField software. Conventional FEA tools often require steep learning curves, substantial computational resources, and costly licenses, thereby limiting their accessibility for both researchers and industry practitioners. QuickField software offers a cost-effective, user-friendly tool for electromagnetic field simulation. It is an alternative for reliable FEA with robust capabilities in modelling complex magnetic, thermal, and electrical phenomena within two-dimensional and three-dimensional domains. It facilitates automated meshing, built-in electromagnetic solvers, and intuitive contour and integral calculation tools that enable researchers to extract detailed performance parameters, including flux density distribution, flux linkage, torque, and inductance, without extensive programming. This accelerates the design iteration process while maintaining computational accuracy [22]. QuickField software was used to perform the FEA of an SMPMM simulating actual B-H curve data for a laminated steel stator and rotor. The simulation investigates key performance indicators, magnetic flux distribution, air-gap flux density, torque, and inductance at 3000 rpm, and compares the results to those presented by Urabinahatti et al. [23], on the magnetic characterization of ferromagnetic alloys for high-speed electric machines. This approach not only improves model reliability but also demonstrates the capability of QuickField as a cost-effective yet precise simulation tool for high-speed permanent magnet machine design.

This research aims to simulate the FEA model of an SMPMM by solving Maxwell's equations on meshed geometries of the SMPMM to obtain the nonlinear magnetic properties of laminated electrical steels using QuickField software. The specific objectives of this study are to simulate the B–H curve data for laminated steel stator and rotor materials, to evaluate the magnetic flux distribution, air-gap flux density, torque, as well as self- and mutual inductances at an operational speed of 3000 rpm, and to compare the simulated results with available experimental data. The following section presents the materials and methods adopted to achieve these objectives.

2. Materials and methods

2.1 Geometry and motor design

A two-dimensional cross-sectional model for the SMPMM, shown in Figure 1, was designed to accurately represent the radial distribution of the magnetic flux. The key design parameters, as presented in Table 1, include a stator with an outer diameter of 125 mm, an inner diameter of 45.6 mm, and nine slots. The rotor possesses an outer diameter of 44.7 mm, with an air gap of 0.45 mm separating it from the stator. This air gap is pivotal in balancing the magnetic performance and mechanical reliability; it is sufficiently narrow to ensure robust magnetic coupling and high flux density for efficient torque generation, yet wide enough to prevent mechanical contact and accommodate manufacturing tolerances. The rotor is fitted with surface-mounted permanent magnets, each 7.5 mm thick, spanning a mechanical angle of 55°, and the shaft diameter measures 18 mm. Each phase winding consists of 1,458 conductors, and the motor stack length is 38 mm.

2.2 Finite element analysis experimental setup

The electromagnetic characteristics of the SMPMM were simulated using QuickField software. A two-dimensional (2D) magnetostatic FEA was utilized to determine the steady-state magnetic field distribution, flux linkage, and inductance, while a time-stepping transient FEA was employed to model the rotor movement at 3000 RPM and to identify speed-related losses. The analysis encompassed the entire cross-section of the stator, rotor, air gap, permanent magnets, and shaft, with meshing and material properties.

Table 1: Geometric and material parameters of the SMPMM

Stator Data		**Rotor Data**	
Stator external diameter	125.0 mm	Rotor external diameter	44.7 mm
Stator inner diameter	45.60 mm	Shaft diameter	18.0 mm
Stack length	38.00 mm	**Permanent Magnet Data**	
Number of poles	2P=6	Permanent magnet thickness	7.5 mm
Number of slots	9	Mechanical permanent magnet angle	55 deg
Number of series conductors per phase	1458	Residual flux density	0.4 T
Stator Slot Data			
Width of the slot opening	3.55 mm		
Width of the stator tooth	7.50 mm		
Height of slot opening	4.00 mm		
Total height of the slot	22.0 mm		

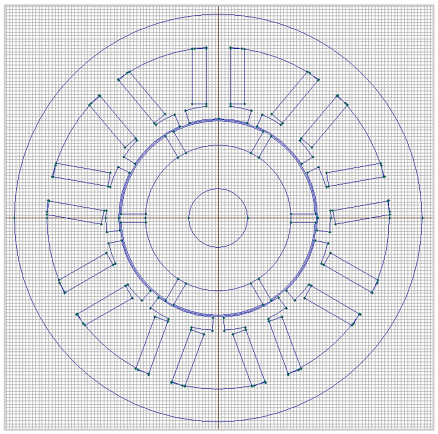

Figure 1: Surface-mounted permanent magnet motor geometry

2.3 Material properties

The stator and rotor cores were designed using ferrite permanent magnets owing to their affordability and outstanding thermal stability. To adequately simulate the magnetic characteristics, the B-H curves were included directly in the simulation, allowing for the description of nonlinear magnetic permeability and saturation processes.

2.4 Meshing and discretization

Accurately quantifying electromagnetic characteristics under dynamic situations is a major challenge [24]. A significant aspect of this method is that it requires splitting the motor geometry into a finite number of elements for the simulation. The ability of triangular finite elements to provide high precision while maintaining sufficient computational accuracy leads to their selection from several types of elements [24,25]. The QuickField software was used for automated meshing, which dynamically modified the element sizes and node distributions according to the field gradients. The mesh refinement focused on regions demonstrating high magnetic field changes, notably near the stator teeth, air gap, and magnetic contacts. Smaller elements were automatically placed in regions where precision was crucial. The mesh convergence was verified, and attempts were made to resolve any element intersection difficulties to ensure reliable simulation results. The SMPMM meshing process (illustrating transition from the original unmeshed geometry) of the positive and negative coils A, B and C is shown in Figure 2, while the fully meshed model of the stator, rotor, air gap, and shaft of the permanent magnets is shown in Figure 3. This illustrates the conceptualized geometric model required for precise field analysis.

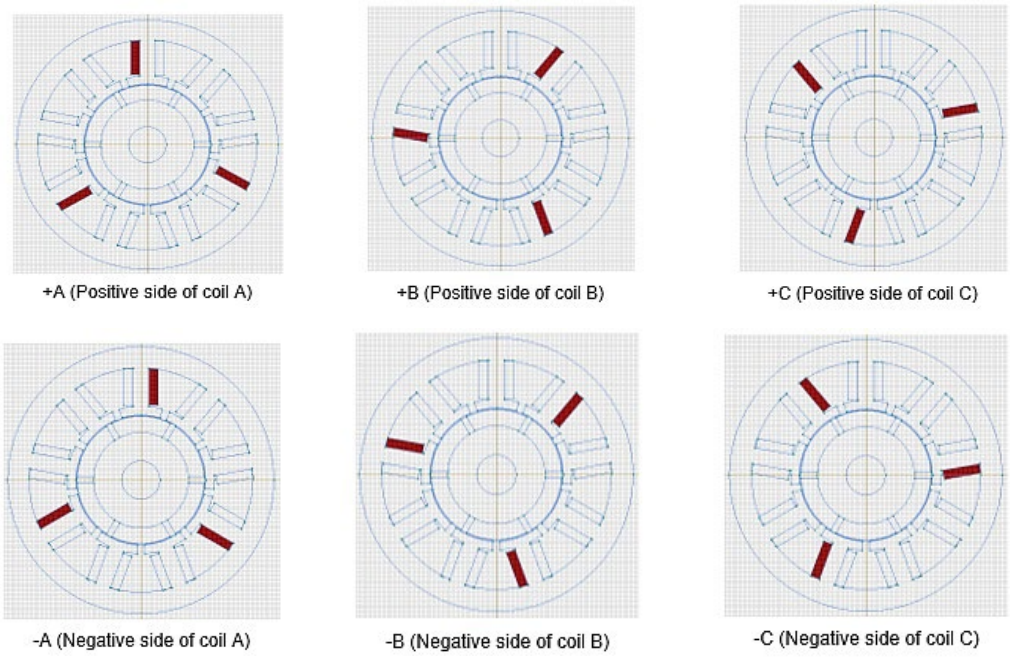

Figure 2: Geometrical model of positive and negative coils A, B, and C

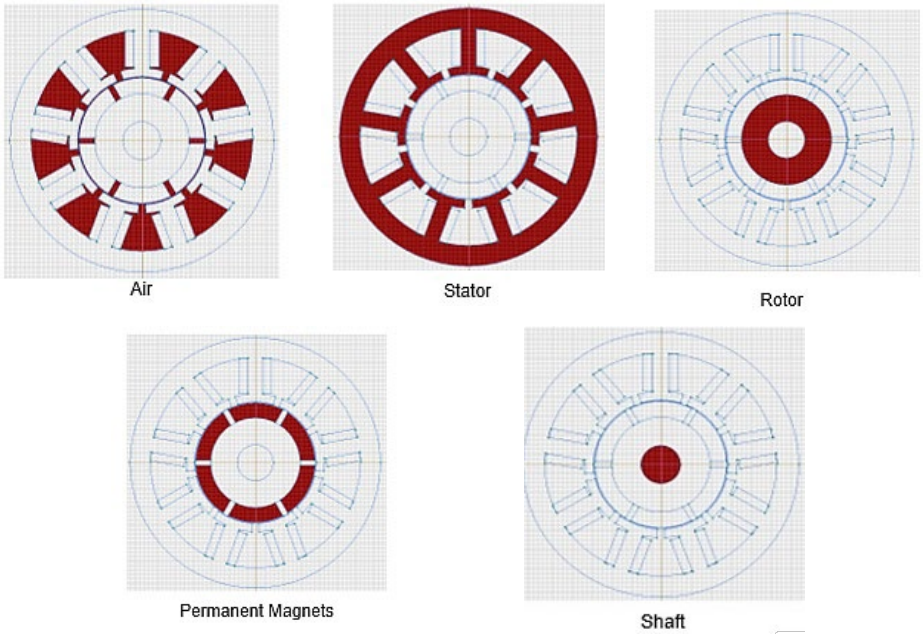

Figure 3: Geometrical model of air, stator, rotor, permanent magnets, and shaft

2.5 Boundary conditions

The two-dimensional solution of Maxwell's equations was analyzed using Dirichlet and Neumann boundary conditions. The magnetic vector potential equation offers a reliable method for illustrating the magnetic field distribution, as shown in Figure 4.

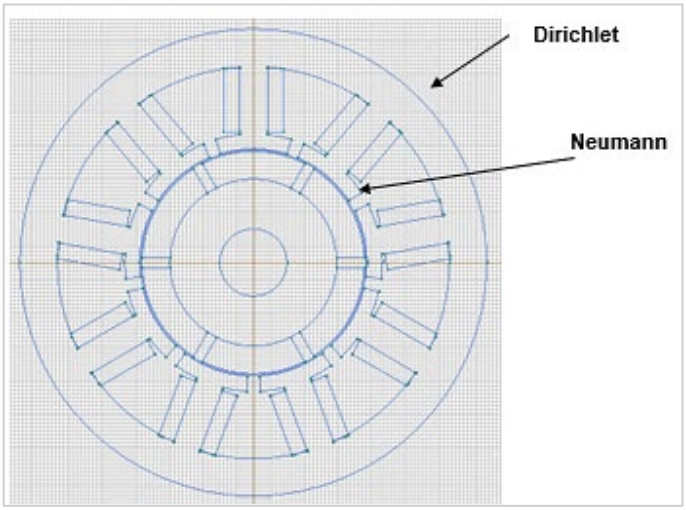

Figure 4: Dirichlet and neumann boundary conditions

Dirichlet boundary conditions were implemented on the outer surfaces of the simulation area to establish a constant magnetic vector potential, effectively simulating ground magnetic field boundaries and confining the field within the computational region [26]. Neumann boundary conditions were applied throughout the air gap to guarantee the natural continuity of the magnetic field and to aid in analyzing variations in the magnetic scalar potential within the clearance [26].

2.6 Development of the model

Finite element analysis based on Maxwell's equations was used to simulate the electromagnetic behaviour of the SMPMM. The analysis applied magnetostatic equations to model steady-state magnetic fields, capturing the flux distribution, residual magnetization, and nonlinear material properties. The magnetostatics equations are shown in Equations (1-9).

$$curlH = J \tag{1}$$

$$divB = 0 \tag{2}$$

The relationship between the magnetic flux density B and the magnetic field intensity H is given by Equation (3):

$$B = B_{res} + \mu H \tag{3}$$

where: $B_{res} =$ residual flux density; μ=permeability of the magnet.

The permeability μ is defined as $\mu = \mu_r \mu_0$. Thus,the magnetic flux Equation (3) becomes:

$$B = B_{res} + \mu_r \mu_0 H \tag{4}$$

where B_{res} represents the residual flux-density vector of the permanent magnet.

$$B_{res} = \left(B_{res,x}, B_{res,y}\right) \tag{5}$$

As the divergence of a *curl* is always zero, Recall Equation (1) and (2)

$$div(curlB) = 0, \text{ and } divB = 0 \tag{6}$$

It is possible to define a magnetic vector potential A so that,

$$B = curlA \tag{7}$$

Substituting equations (4), and (5) into the curl equation, we obtain:

$$curlH = curl\left(\frac{B - B_{res}}{\mu_r \mu_0}\right) = curl\left(\frac{B}{\mu_r \mu_0}\right) - curl\left(\frac{B_{res}}{\mu_r \mu_0}\right)$$

which simplifies into:

$$curlH = curl\frac{1}{\mu}(CurlA) - curl\left(\frac{B_{res}}{\mu_r \mu_0}\right) = J \tag{8}$$

where: B_{res} is the residual flux density vector of the permanent magnet, and μ_r and μ_0 are the relative and absolute permeabilities, respectively.

For a two-dimensional model in the (x, y) plane, both the magnetic vector potential A and current density J are assumed to have z-axis components. Therefore, vector A is parallel to vector J. The vectors can be expressed as $J = [0, 0, J_z]$, and $A = [0, 0, A]_z$. Under this assumption, the magnetic field
is restricted to the xy plane, and the governing electromagnetic field equation derived from Maxwell's equations simplifies accordingly. Based on these conditions, the governing partial differential equation becomes:

$$\frac{\partial}{\partial x}\left(\frac{1}{\mu_r}\frac{\partial A_z}{\partial x}\right) + \frac{\partial}{\partial y}\left(\frac{1}{\mu_r}\frac{\partial A_z}{\partial y}\right) = -\mu_0 J_z - \frac{\partial}{\partial x}\left(\frac{B_{res,y}}{\mu_r}\right) + \frac{\partial}{\partial y}\left(\frac{B_{res,x}}{\mu_r}\right) \tag{9}$$

This equation defines how the motor meshing domain, incorporating material properties along with Dirichlet and Neumann boundary conditions, influences the spatial distribution of the magnetic vector potential (A_z) as a result of magnetization (B_{res}), permeability (μ_r), and applied current (J_z). These factors directly affect the flux linkage, torque production, and core saturation in the SMPMM.

A time-stepping transient analysis was conducted to model current excitations ranging from 0 to 2 A. The simulation was based on the actual motor geometry, which included the stator, rotor, shaft, and surface-mounted magnets. The finite element mesh was designed using triangular elements with adaptive refinement applied to areas with significant field gradients. The geometries that were meshed and those that were not are shown in Figures 5(a) and 5(b), respectively. Figure 5(b) further demonstrates the distribution of the magnetic field intensity, emphasizing the regions with a high flux concentration.

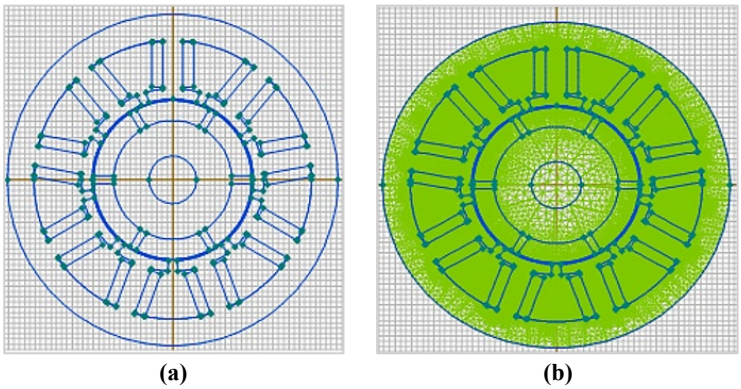

(a) **(b)**

Figure 5: Unmeshed and meshed geometries of the SMPMM

2.7 Flux linkage and inductance analysis

The flux linkage and inductance were determined by assessing the self-and mutual inductances inside the electromagnetic field of the SMPMM. These characteristics were obtained based on the total magnetic flux passing through the conducting loop within the meshed geometry of the motor. The finite element equation analyzes the influence of magnetic saturation and current excitation on the inductance behaviour. The flux linkage in the coil is expressed by Equation 8 [27].

$$\varphi_k = L_{kk}.i_k + \sum_n M_{nk}.i_n \quad (8)$$

where :L_{kk} = Self-inductance of the coil k, M_{nk} = Mutual inductance between coil n and k, i_n = Current in the coil n, i_k = Current in the coil k.

Additionally, the stored magnetic energy, which is a function of the current and inductance, is given by [28]:

$$W = \frac{1}{2}\left(\sum_k^k L_{kk} i_k^2 + \sum_n^k M_{nk} i_n i_k\right) \quad (9)$$

Inductance can be derived using Equation (10):

$$L = \frac{\varphi}{i} \quad (10)$$

where ϕ is the flux linkage and I is the current. Alternatively, the inductance can be determined from the stored magnetic energy as shown in Equation (11):

$$L = \frac{2W}{i^2} \quad (11)$$

where W represents the stored magnetic energy, and i is the current in the system.

2.8 High-field nonlinear magnetic analysis

Most SMPMM studies restrict magnetic modeling to flux densities around 1.8 Tesla (T), which is the typical threshold for core saturation in electrical steels. However, during transient overloads, fault conditions, or peak torque demands, localized flux densities can surpass this limit. To fully capture the nonlinear behavior of the SMPMM, the B–H curve of M36 laminated steel was extended to 2.75 T using high-field data from manufacturer datasheets. This extension enabled the finite element model to accurately depict the sharp decline in magnetic permeability that occurs beyond 1.8 T. By incorporating these extended material characteristics, the FEA simulations could assess the motor's performance under both normal operating conditions and extreme scenarios where deep saturation effects significantly impact magnetic coupling, torque production, and loss mechanisms.

3. Results and discussion

3.1 Magnetic field distribution of the stator, rotor, and permanent magnet

As shown in Figure 6, the magnetic field distribution was stimulated to a maximum current of 2A. The B-H curve of the laminated steel used for the stator and rotor components demonstrated a nonlinear magnetic response across the applied field range. Initially, the curve increased steeply from 1.3 Tesla (T) to 1.42T, signifying a region of high magnetic permeability where the material is easily magnetized under low excitation. This high initial permeability is essential for electric motors, as it reduces the magnetizing current and minimizes core losses, thereby enhancing the overall energy efficiency and facilitating strong magnetic coupling between the stator and rotor. Beyond 1.42T, the curve begins to flatten as the magnetic field intensity increases from 0 to 57,000 A/m, ultimately reaching saturation near 2.75T. This nonlinear behaviour indicates the onset of magnetic saturation, where a further increase in the magnetic field strength yields only minimal changes in flux density. In this region, the magnetic domains of the material are predominantly aligned, resulting in reduced effective permeability and diminished responsiveness to the magnetising force, a phenomenon often referred to as magnetic rigidity. This behaviour is consistent with the findings of Szabó and Weber [29], who observed that laminated electrical steel is extensively utilised in motor applications owing to its high initial permeability and low hysteresis losses, which significantly enhance the dynamic efficiency of the SMPMM [30-32].

The B-H curve for the ferrite permanent magnet driving the rotor is shown in Figure 7. The chart demonstrates a relatively linear relationship between the magnetic field strength and flux density, starting from 0 A/m and increasing to a peak flux density of 0.44 T. The magnetic flux density reduces to approximately 0.03 T when the field intensity drops to –240,000 A/m. Unlike laminated steels, ferrite magnets do not exhibit saturation areas. This linear trend is characteristic of materials with relatively low magnetic permeability [32, 33]. The linear response of the ferrite magnet implies consistent performance across different field intensities, making it suitable for applications in which soft magnetic behaviour is required [34-36].

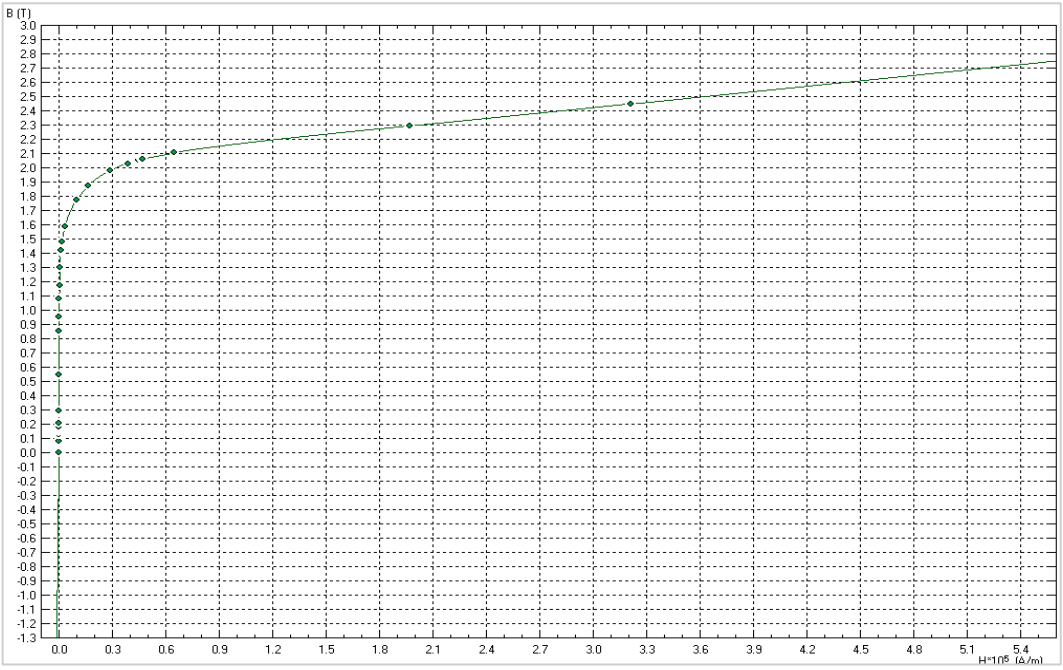

Figure 6: B-H curve of lamination steel used for stator and rotor

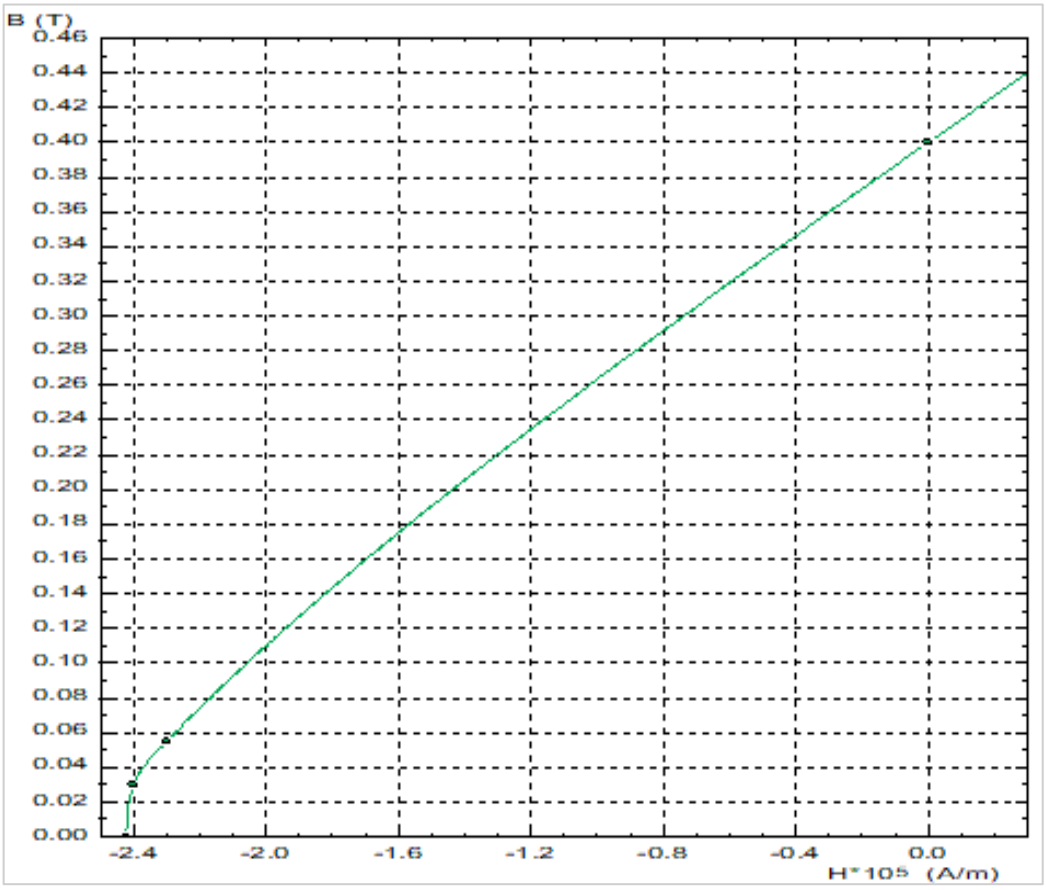

Figure 7: B-H curve of permanent magnet (ferrite)

3.2 Magnetic flux distribution in the SMPMM

The magnetic field distribution and flux density color map of the simulated ferrite-based SMPMM is shown in Figures 8(a) and 8(b), respectively. These visualizations illustrate the electromagnetic properties of the motor during full-current excitation. The line is the track of the magnetic field concentration around the magnets and stator, whereas the magnetic flux density (B) within the SMPMM is represented by the color map in Figure 8b. Denser magnetic flux regions appear in red and yellow, indicating that the magnetic field around the permanent magnets and stator teeth is high. The less dense magnetic flux region of the SMPMM is the air gap, and some less magnetic areas appear in blue and purple. The high concentration of magnetic flux

lines near the rotor and stator indicates an effective magnetic circuit design. This region, showing an abnormally high magnetic flux density, may signify potential material saturation, hence the need for design optimization. The homogeneous distribution of the flux in the stator indicates effective electromagnetic performance.

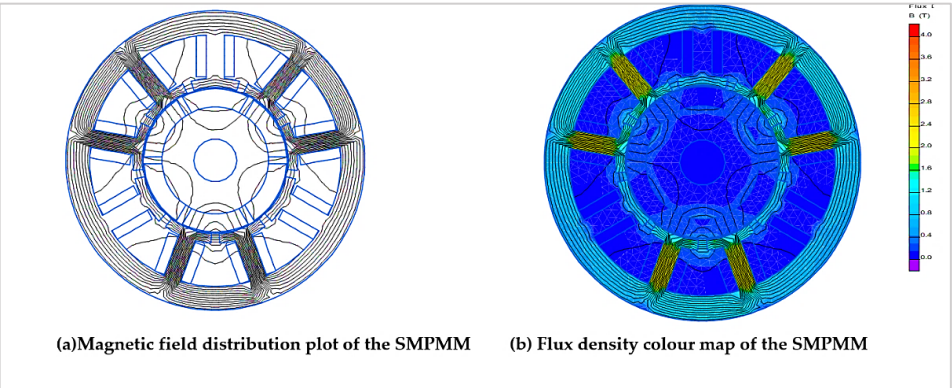

Figure 8: Magnetic field distribution a) and flux density color map b) of the SMPMM

3.3 Magnetic flux density distribution in the air-gap of the SMPMM

Figure 9 illustrates the distribution of the magnetic flux within the SMPMM air gap, which is the radial clearance between the rotor and stator. This graph shows how the magnetic flux density (B) fluctuates over the air gap as a function of rotor location. The waveform reveals periodic peaks that correspond to fluctuations in the flux density during rotor rotation. These peaks represent the alternating nature of the magnetic field created by the permanent magnets. The number of peaks detected in every electrical cycle is correlated with the number of pole pairs in the magnet [37]. Thus, magnets with more pole pairs display a higher number of flux-density oscillations within a given rotation. The peak amplitudes, generally ranging from 0.7 T to 1.2 T, indicate the greatest magnetic flux densities encountered in the air gap [38]. These numbers are crucial for analyzing the electromagnetic performance of machines. A well-distributed air-gap flux density contributes to reduced torque ripple, minimal core losses, and lower electromagnetic noise factors that directly impact the smoothness and efficiency of the motor.

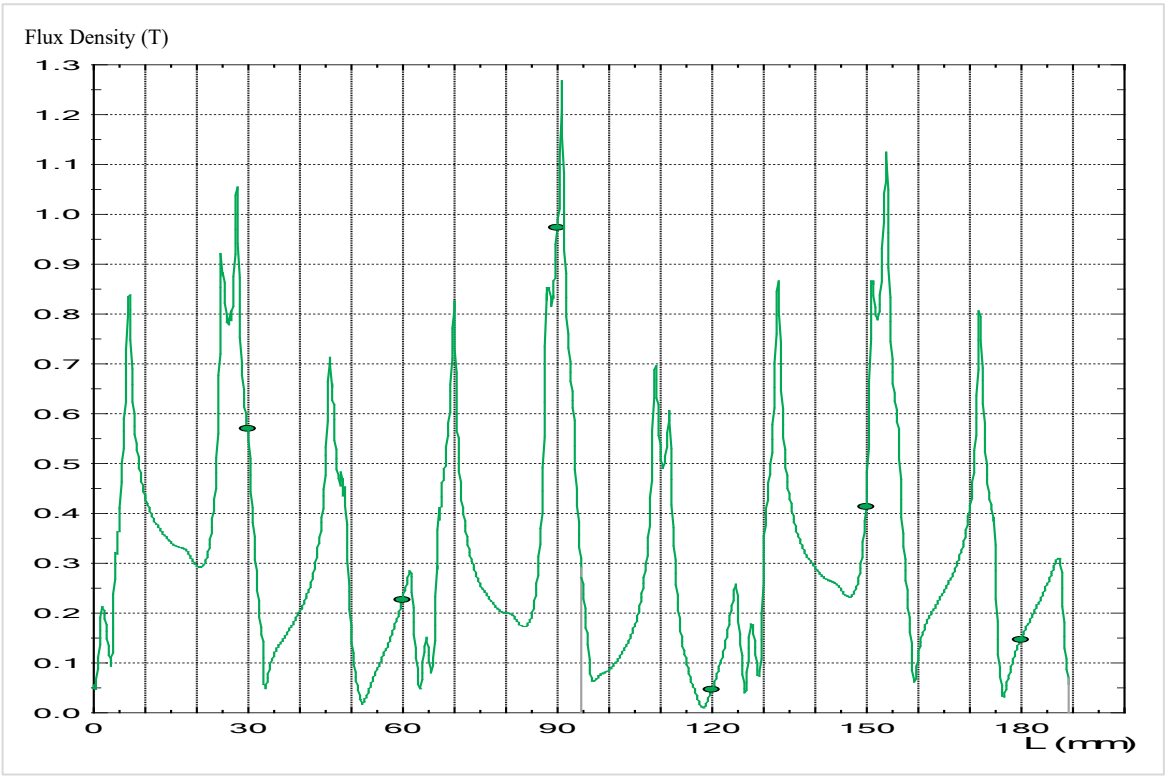

Figure 9: Air gap magnetic flux density distribution on SMPMM

3.4 Flux linkage

The flux linkage of the SMPMM was observed with a current loading from 0 A to a rated current of 2 A in phase A, as shown in Figure 10. The results show a nonlinear increase in the flux linkage as the current increases from 0 to 2 A. The curve initially appears linear at lower currents; however, as the current increases to 2 A, the flux linkage begins to bend and reaches

magnetic saturation. This magnetic saturation is due to reduced material permeability, which limits the flux linkage [39], and responsible for the demagnetization of the SMPMM.

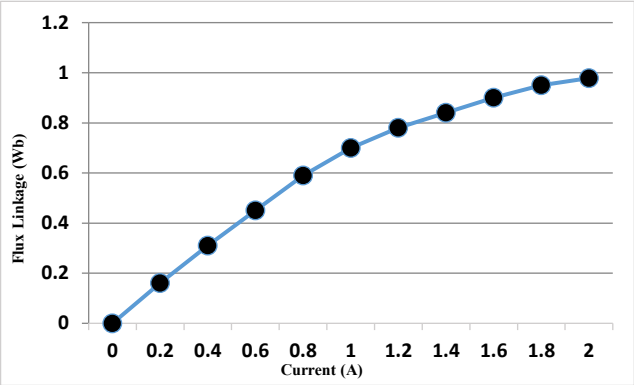

Figure 10: Flux linkage versus current in Phase A

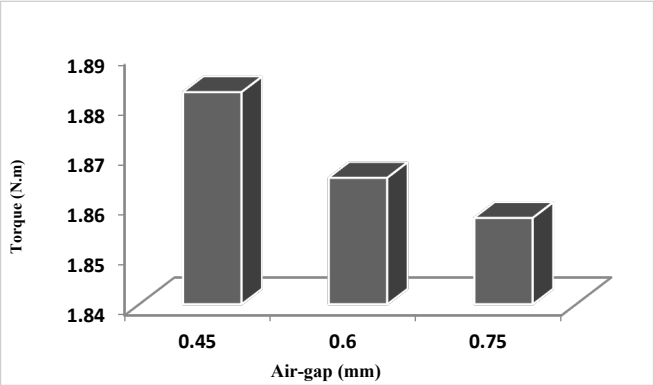

Figure 11: Torque versus air-gap length bar chart

3.5 Torque interaction with the air-gap

The torque generated by the interaction between the permanent magnets of the rotor and stator currents is shown in Figure 11. This interaction is influenced by the air gap (clearance between the rotor and stator of the magnetic motor). The figure shows that the torque values decreased from 1.8823 N.m at 0.45 mm to 1.8572 N.m at 0.75 mm. This indicates that a higher torque was generated in the small air gaps owing to the strong magnetic coupling in the simulated magnet. These results agree with those of Ebot and Fujimoto [40] and Zhou et al. [41], who showed that optimizing the air-gap dimensions, controlling currents, and preventing magnetic saturation are essential for achieving efficient and reliable motor performance for the magnetic motor.

3.6 Self-inductance of the SMPMM

Figure 12 shows the relationship between the self-inductance (H) and current (I) in the simulated magnetic motor. At low current excitation between 0.2 A and 0.6 A, the self-inductance of the magnet is relatively stable (0.8 H), showing that the magnetic material is operating in its high-permeability area. However, when the current excitation increases above 0.6 A, the inductance begins to drop, showing the onset of magnetic saturation in the core material. This pattern continued when the current approached 1 A, with a considerable decline in the inductance. At a maximum excitation of 2 A, the self-inductance drops to 0.5 H. This decline demonstrates that increasing the current levels moves the magnetic core toward saturation, resulting in lower permeability and energy storage capabilities. These findings emphasize the nonlinear electromagnetic behaviour of the SMPMM.

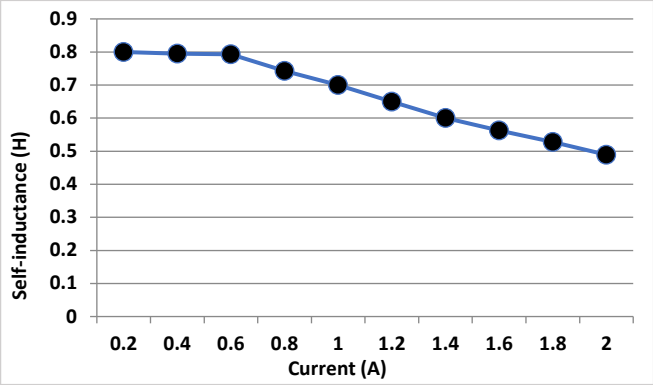

Figure 12: Self-inductance versus current

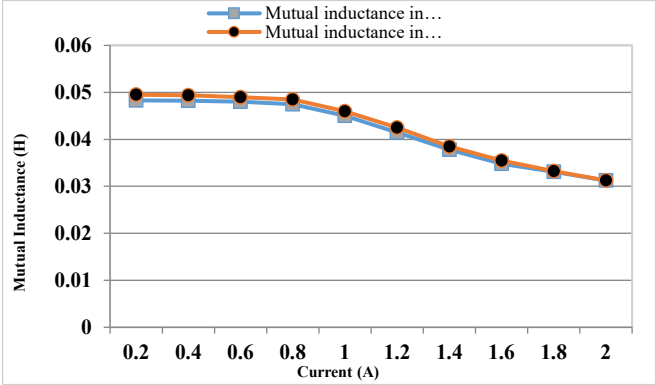

Figure 13: Mutual Inductance versus current

3.7 Mutual inductance of the SMPMM

Figure 13 illustrates the relationship between the mutual inductance (H) and current (A) in two coil pairs (A, B, and A, C) of a surface-mounted permanent-magnet motor. At 0.2 A, the mutual inductance for coils A and B, and A and C, is 0.048 H and 0.049 H, respectively, which remains virtually constant up to 0.8 A. Beyond 1 A, mutual inductance begins to reduce, with a notable drop at 1.2 A, when coils A and B fall to 0.038 H, while coils A and C are somewhat higher at 0.039 H. As the current increases, the mutual inductance drops swiftly to 0.03 H at 2 A for both coil pairs. This pattern demonstrates magnetic saturation effects, which lower the permeability and alter the flux linkage. The slightly larger mutual inductance in coils A and C compared to coils A and B implies changes in the magnetic interactions. This decrease in mutual inductance at higher currents influences motor performance.

3.8 Motor speed and loss consideration

The operational speed of the SMPMM is a significant component in determining the loss performance, particularly under high-frequency excitation situations. For this investigation, the motor was simulated at a nominal speed of 3000 RPM, which indicates a normal industrial working point. At higher speeds, an increase in the magnetic field cycle rate increases the core and eddy current losses, particularly in laminated materials with lower resistivity. Core loss analysis was introduced into the simulation by linking the magnetic flux density fluctuation with frequency-dependent loss models. At increasing flux densities and rotating speeds, eddy current losses increased nonlinearly because of the increased magnetic field gradients and lower permeability under saturation. This demonstrates the importance of sophisticated loss modelling for properly estimating the thermal and efficiency parameters under dynamic, high-speed operation.

4. Validation of FEA of the electromagnetic field

The electromagnetic field performance of the SMPMM was compared to the magnetic characterization of ferromagnetic alloys for high-speed electric machines [23]. This research provides a dependable foundation for corroborating the fundamental magnetic properties identified in the FEA of SMPMM using QuickField.

4.1 Magnetic field distribution at maximum current (2A)

The magnetic field distribution in the SMPMM at a current excitation of 2 A is consistent with the experimentally derived B-H properties of the M36 laminated steel. Urabinahatti et al. [23] report that M36 shows a sharp initial rise in flux density, signifying enhanced permeability, and eventually saturates beyond approximately 1.4 T at magnetic field intensities exceeding 20,000 A/m. This trend aligns with the modelling results shown in Figure 6, where the B-H curve levels off after 1.42 T, signifying magnetic saturation. The simulated response demonstrates that laminated steel is appropriate for reducing hysteresis losses and guaranteeing effective magnetisation, which are two qualities essential for SMPMM stator cores.

4.2 Magnetic properties of the ferrite permanent magnet

The B-H response of the ferrite permanent magnet used in the simulation shows that the magnetic flux density increased linearly from 0 to 0.44 T as the magnetic field intensity increased. Although this trend does not directly validate the study, it complements the findings on the low permeability of the materials. shows that the materials are perfect for predictable and stable operation under dynamic field variations because they show linear and unsaturated B-H properties that characterise soft magnetic behaviour [23].

4.3 Magnetic flux distribution and air gap analysis

The magnetic flux density distribution in the SMPMM showed a peak range of 0.7 T to 1.2 T within the air gap, which is in line with the saturation levels observed in the laminated materials that were tested (such as M36 and 65C600) at frequencies up to 500 Hz. The flux concentration close to the rotor and stator teeth in Figure 8 matches the colour maps of the flux density shown in the study by Urabinahatti [23], where high saturation was observed along the edges of the laminated steel toroidal cores. The non-uniform field in the air gap also supports the results of skin-effect-based flux redistribution at greater frequencies based on finite elements, particularly for solid cores and EN8.

4.4 Flux linkage and magnetic saturation

The nonlinear flux linkage in the SMPMM increased as the current increased from 0 A to 2 A, which is consistent with the B-H loops of the laminated cores, as shown in Figure 10. The empirical model shows that loop distortion and saturation behaviour were visible above 1 T for M36 and 65C600, with flux linkage characteristic bending under high excitation owing to diminishing permeability. This verifies the simulation conclusion that magnetic saturation becomes evident near the rated current values, thereby influencing flux-linkage nonlinearity.

4.5 Torque interaction with air gap

Magnetic flux concentration around the stator and rotor teeth is experimentally validated, supporting the reported torque drop with increasing air-gap clearance from 1.8823 N.m at 0.45 mm to 1.8572 N.m at 0.75 mm (See Figure 11). The experimental flux maps showed similar high-density zones next to the magnetic poles, indicating effective coupling in minimal air-gap arrangements. This validates the basis for the increased torque generation at smaller air gaps in the FEA of the simulated SMPMM.

4.6 Self-inductance and mutual inductance

The simulated self-inductance exhibits a stable response at low currents, declining from 0.8 H to approximately 0.5 H as the current increases to 2 A. The reduced permeability and magnetic saturation are consistent with the empirical simulation findings of U. The declining mutual inductance with increasing current, from 0.049 H to 0.03 H, is consistent with the reduction in the induced saturation in effective magnetic coupling, as observed experimentally in solid cores such as EN8 and hardened EN353, where saturation significantly distorted the B-H loops and reduced magnetic responsiveness.

5. Conclusion

This paper presented a finite element analysis of the electromagnetic field of an SMPMM using QuickField software, evaluating the nonlinear magnetic saturation, dynamic current excitation, and speed-dependent electromagnetic losses. The simulation utilized laminated steels for the stator and rotor cores and ferrite magnets as the permanent magnetic material at an operational speed of 3000 RPM. Under rated current excitation, the study highlights key electromagnetic performance metrics, such as magnetic field distribution, flux linkage, torque interaction with the air gap, self-inductance, and mutual inductance.

Field plots revealed high flux concentrations around the stator teeth and magnets, suggesting effective magnetic circuit design but also identifying regions prone to localized saturation. The simulated air-gap flux density ranged from 0.7 T to 1.2 T, aligning with pole-pair geometry and essential for controlling torque ripple and minimizing core losses. Flux linkage increased from 0.02 Wb to 0.065 Wb with current, while transient simulations showed peak torque of 1.8823 N.m at a 0.45 mm air gap, slightly decreasing to 1.8572 N.m at 0.75 mm. Self-inductance dropped from 0.8 H to 0.5 H, and mutual inductance declined from 0.049 H to 0.03 H, reflecting reduced magnetic coupling under saturation. These results, validated against experimental data from literature, confirm the model's accuracy and underscore the importance of incorporating both nonlinear magnetic characteristics and speed-dependent loss mechanisms in SMPMM design. The dual FEA approach offers a more comprehensive understanding of steady-state and dynamic behavior, facilitating the development of high-efficiency, high-reliability motors for demanding industrial, automotive, and renewable energy applications.

Author contributions

Conceptualization, **T. Ayorinde** , **P. Roux** , and **T. Jamiru**; data curation, **P. Roux**; formal analysis, **P. Roux**; investigation, **P. Roux**; methodology, **P. Roux** and **T. Ayorinde**; project administration, **P. Roux**, and **T. Ayorinde**; resources, **T. Jamiru**; software, **P. Roux** and **T. Ayorinde**; supervision, **P. Roux**, and **T. Jamiru**; validation, **T. Ayorinde**; visualization, **P. Roux**, and **T. Ayorinde**; writing—original draft preparation, **T. Ayorinde**; writing—review and editing, **T. Ayorinde**, **P. Roux**, and **T. Jamiru**; All authors have read and agreed to the published version of the manuscript.

Funding

This research received no specific grants from any funding agency in the public, commercial, or not-for-profit sectors.

Data availability statement

The data that support the findings of this study are available upon request from the corresponding author.

Conflicts of interest

The authors declare that there is no conflict of interest.

References

[1] S. S. Kamble, A. Gunasekaran, S. A. Gawankar, Sustainable Industry 4.0 framework: A systematic literature review identifying the current trends and future perspectives, Process Saf. Environ. Prot., 117 (2018) 408-425. https://doi.org/10.1016/j.psep.2018.05.009

[2] Q. Jiang, C. Bi, R. Huang, A new phase-delay-free method to detect back EMF zero-crossing points for sensorless control of spindle motors, IEEE Trans. Magn., 41 (2005) 2287-2294. https://doi.org/10.1109/TMAG.2005.851841

[3] Z. Qingjie, Z. Yanqing, Scheme design of high performance converting control of linear induction motor used for electromagnetic launch, IEEE 16th International Symposium on Electromagnetic Launch Technology, Beijing, China, 2012, 1-4. https://doi.org/10.1109/EML.2012.6511067

[4] Zhang, X. Electromagnetic performance analysis of surface-mounted permanent magnet machine. Bachelor's Thesis, 2024.

[5] R. Qu, Y. Zhou, D. Li, Milestones, hotspots and trends in the development of electric machines, iEnergy, 1 (2022) 82-99. https://doi.org/10.23919/IEN.2022.0002

[6] W. Zhang, G.J. Li, Z.Q. Zhu, B .Ren, Y.C. Chong, Coupled Electromagnetic–Thermal Modelling of Dynamic Performance for Modular SPM Machines, Energies, 16 (2023) 2516. https://doi.org/10.3390/en16062516

[7] Littera, D. Investigation of PM Formation and Evolution in Plumes Emitted by Heavy-Duty Diesel Vehicles: Wind Tunnel Study; West Virginia University, 2014.

[8] Hendershot, J. R. and Miller, T. J. E. Design of brushless permanent-magnet motors; Oxford university press, 1995.

[9] H. M. C. Beigi, M .Cheshmeh, Design, optimization and fem analysis of a surface-mounted permanent-magnet brushless dc motor, Int. J. Eng., 31 (2018) 339-345.

[10] X. Ba, Z. Gong, Y. Guo, C. Zhang, J. Zhu, Development of equivalent circuit models of permanent magnet synchronous motors considering core loss, Energies, 15 (2022) 1995. https://doi.org/10.3390/en15061995

[11] K. T. Chau, C. C. Chan, C. Liu, Overview of permanent-magnet brushless drives for electric and hybrid electric vehicles, IEEE Trans. Ind. Electron., 55 (2008) 2246-2257. https://doi.org/10.1109/TIE.2008.918403

[12] Z. Q. Zhu, D. Howe, Electrical machines and drives for electric, hybrid, and fuel cell vehicles, Proceedings of the IEEE, 95, 2007, 746-765. https://doi.org/10.1109/JPROC.2006.892482

[13] K. Guo, H. Lu, G.J. Xu, D. Liu, H. B. Wang, X. M. Liu, X. Y. Song, Recent progress in nanocrystalline Sm–Co based magnets, Mater. Today Chem., 25 (2002) 100983. https://doi.org/10.1016/j.mtchem.2022.100983

[14] A. Usman, A. Saxena, Technical Roadmaps of Electric Motor Technology for Next Generation Electric Vehicles, Machines, 13 (2025) 156. https://doi.org/10.3390/machines13020156

[15] B. Rezaei, H. E. J. Moni, I. H. Karampelas, Additive Manufacturing of Magnetic Materials for Energy, Environment, Healthcare, and Industry Applications, Adv. Funct. Mater., 35 (2025) 2416823. https://doi.org/10.1002/adfm.202416823

[16] S. O. Altiparmak, K. Waters, C. G. Thies, Cornering the market with foreign direct investments: China's cobalt politics, Renewable and Sustainable Energy Transition, 7 (2025) 100113. https://doi.org/10.1016/j.rset.2025.100113

[17] S. Islam, H. Weerasinghe, D. M. Prado, A. N. Gonzaga, C. Burda, Diversifying the Materials and Technologies for the Future of Energy Storage, Energy Fuels, 39 (2025) 8369–8390. https://doi.org/10.1021/acs.energyfuels.5c00468

[18] W. Sun, H. Si, J. Qiu, J. Li, Research on Efficiency of Permanent-Magnet Synchronous Motor Based on Adaptive Algorithm of Fuzzy Control, Sustainability, 16 (2024) 1253. https://doi.org/10.3390/su16031253

[19] G. R. SLEMON, On the design of high-performance surface-mounted PM motors, IEEE Trans. Ind. Appl., 30 (1994) 134-140. https://doi.org/10.1109/28.273631

[20] P. König, D. Sharma, K. R .Konda, T. Xie, K. Höschler, Comprehensive review on cooling of permanent magnet synchronous motors and their qualitative assessment for aerospace applications, Energies, 16 (2023) 7524. https://doi.org/10.3390/en16227524

[21] Müller, G. and Ponick, B. Grundlagen elektrischer Maschinen; John Wiley & Sons, 2014.

[22] L. R. Devi, S. Sreekumar, R. Bhakar, G. Dileep, S. Padmanaban, Electric motor modeling, analysis, and design for E-mobility applications: A state of the art, e-Prime-Advances in Electrical Engineering, Electronics and Energy, 12 (2025) 100985. https://doi.org/10.1016/j.prime.2025.100985

[23] C. Urabinahatti, S.S. Ahmad, G. Narayanan, Magnetic characterization of ferromagnetic alloys for high-speed electric machines, IEEE Trans. Ind. Appl., 56 (2020) 6436-6447. https://doi.org/10.1109/TIA.2020.3023868

[24] M. Yilmaz, Limitations/capabilities of electric machine technologies and modeling approaches for electric motor design and analysis in plug-in electric vehicle applications, Renewable and Sustainable Energy Reviews, 52 (2015) 80-99. https://doi.org/10.1016/j.rser.2015.07.033

[25] B. Bilgin, J. Liang, M. V. Terzic, J. Dong, R. Rodriguez, E. Trickett, A .Emadi, Modeling and analysis of electric motors: State-of-the-art review, IEEE Trans. Transp. Electrif., 5 (2019) 602-617. https://doi.org/10.1109/TTE.2019.2931123

[26] Bianchi, N. 2005. Electrical machine analysis using finite elements, Taylor & Francis Group Logo,Vol.7, pp. 304: CRC press. https://doi.org/10.1201/9781315219295

[27] N. K. Sheth, K. R. Rajagopal, Calculation of the flux-linkage characteristics of a switched reluctance motor by flux tube method, IEEE Trans. Magn., 41 (2005) 4069-4071. https://doi.org/10.1109/TMAG.2005.854865

[28] M. Cheng, W. Qin, X. Zhu, Z. Wang, Magnetic-inductance: Concept, definition, and applications, IEEE rans. Power Electron., 37 (2022) 12406-12414. https://doi.org/10.1109/TPEL.2022.3175372

[29] V. Szabó, K. Weber, A novel method for structural strength modeling of lamination stacks of electric motors using contact in FEA, Results Eng., 26 (2025) 104699. https://doi.org/10.1016/j.rineng.2025.104699

[30] S. Zhu, M. Cheng, J. Dong, J. Du, Core loss analysis and calculation of stator permanent-magnet machine considering DC-biased magnetic induction, IEEE Trans. Ind. Electron., 61 (2014) 5203-5212. https://doi.org/10.1109/TIE.2014.2300062

[31] X. Zhang, Q. Du, J. Xu, Y. Zhao, S. Ma, Development and analysis of the magnetic circuit on double-radial permanent magnet and salient-pole electromagnetic hybrid excitation generator for vehicles, Chin. J. Mech. Eng., 32 (2019) 1-13. https://doi.org/10.1186/s10033-019-0334-x

[32] L. A. Kumar, B. M. Raj, V. Vijayakumar, V. Indragandhi, V. Subramaniyaswamy, H.R. Karimi, Analysis of Electric Motor Magnetic Core Loss under Axial Mechanical Stress, Sensors, 20 (2020) 6818. https://doi.org/10.3390/s20236818

[33] M. Przybylski, D. Kapelski, B. Ślusarek, S. Wiak, Impulse magnetization of Nd-Fe-B sintered magnets for sensors, Sensors, 16 (2016) 569. https://doi.org/10.3390/s16040569

[34] G Choi, Analysis and experimental verification of the demagnetization vulnerability in various PM synchronous machine configurations for an EV application, Energies, 14 (2021) 5447. https://doi.org/10.3390/en14175447

[35] J. Faiz, M.A. Bazrafshan, Z. Tabarniarami, Demagnetisation fault analysis and diagnosis based on different methods in permanent magnet machines-An overview, IET Electr. Power Appl., 18 (2024) 1860-1893. https://doi.org/10.1049/elp2.12519

[36] H. R. Kirchmayr, Permanent magnets and hard magnetic materials, J. Phys. D: Appl. Phys., 29 (1996) 2763. https://dx.doi.org/10.1088/0022-3727/29/11/007

[37] B. Guo, Y. Wu, F. Peng, A Novel Magnetic Permeance Network Model for SPM Machine With Bread-Loaf Structure, IEEE Trans. Ind. Electron., (2025)1-10. https://doi.org/10.1109/TIE.2025.3552263

[38] Y. Wei, P. Wang, R. Nie, S. Xu, J. Liang, J. Si, Analytical Modeling and Optimal Design of Slotted Axial Flux PM Motor With Equidirectional Toroidal Winding, IEEE Trans. Ind. Electron., (2025) 1-11. https://doi.org/10.1109/TIE.2025.3552185

[39] M.M. Tezcan, A.G. Yetgin, A.I. Canakoglu, Investigation of the effects of the equivalent circuit parameters on induction motor torque using three different equivalent circuit models, in MATEC Web of Conferences, EDP Sciences, 157, 2018, 1-11. https://doi.org/10.1051/matecconf/201815701019

[40] B. J. Ebot, Y. Fujimoto, Design and Experimental Analysis of a Novel Coreless Two-Phase Resonant Motor, IEEE Trans. Ind. Electron., (2025)1-11. https://doi.org/10.1109/TIE.2025.3559970

[41] Y. Zhou, H. Yang, S. Luo, X. Hao, Optimization Design for Bionic-Bamboo FPs of Coaxial Magnetic Gear Under Multi-Field Coupling, Progress in Electromagnetics Research C, 153 (2025) 51–59. https://doi.org/10.2528/PIERC24112901